Piezoelectric-Effect-Enhanced Full-Spectrum Photoelectrocatalysis in p–n Heterojunction

Zhirong Liu, Longwei Wang, Xin Yu,* Jian Zhang, Ruiqi Yang, Xiaodi Zhang, Yanchen Ji, Mengqi Wu, Lin Deng, Linlin Li,* and Zhong Lin Wang*

Photoelectrochemical (PEC) water splitting offers a promising strategy for converting solar energy to chemical fuels. Herein, a piezoelectric-effect–enhanced full-spectrum photoelectrocatalysis with multilayered coaxial titanium dioxide/barium titanate/silver oxide (TiO_2/BTO/Ag_2O) nanorod array as the photoanode is reported. The vertically grown nanorods ensure good electron conductivity, which enables fast transport of the photogenerated electrons. Significantly, the insertion of a piezoelectric $BaTiO_3$ (BTO) nanolayer at the p-type Ag_2O and n-type TiO_2 interface created a polar charge-stabilized electrical field. It maintains a sustainable driving force that attract the holes of TiO_2 and the electrons of Ag_2O, resulting in greatly increased separation and inhibited recombination of the photogenerated carriers. Furthermore, Ag_2O as a narrow bandgap semiconductor has a high ultraviolet–visible–near infrared (UV–vis–NIR) photoelectrocatalytic activity. The TiO_2/BTO/Ag_2O, after poling, successfully achieves a prominent photocurrent density, as high as 1.8 mA cm^{-2} at 0.8 V versus Ag/Cl, which is about 2.6 times the TiO_2 nanorod photoanode. It is the first time that piezoelectric $BaTiO_3$ is used for tuning the interface of p-type and n-type photoelectrocatalyst. With the enhanced light harvesting, efficient photogenerated electron–hole pairs' separation, and rapid charge transfer at the photoanode, an excellent photoelectrocatalytic activity is realized.

1. Introduction

Over the past few years, photoelectrochemical (PEC) water splitting has gradually evolved into a new solar energy conversion method of great potential.[1] Since the first discovery of TiO_2 to catalyze the PEC water splitting, several decades of hard work has been devoted to developing highly active metal-oxide semiconductor photocatalysts that may hold great promise in efficient solar energy conversion.[2] To construct an ideal photocatalyst for hydrogen (H_2) production by PEC water decomposition, several conditions must be satisfied: 1) direct contact between photocatalyst and substrate electrode to ensure rapid electron transfer, 2) full-spectrum photocatalysis to realize effective utility of solar energy, and 3) efficient separation and consumption of photogenerated carriers with minimal recombination.[3]

TiO_2 nanorod arrays have been widely investigated as a photoanode for PEC applications due to their unique 1D structure and high surface area, allowing the directional electron transport.[4] However, the low spectral utilization and high recombination rate of photogenerated electron–hole pairs in TiO_2 nanorod arrays severely limit the PEC activities.[5] In order to improve the efficiency of photoelectrocatalysis, many strategies have been developed. Thereinto, a rationally designed p–n heterojunction could not only broaden the wavelength range of light absorption and utilization but also minimize the possible recombination of the solar-separated carriers.[6] The construction of p–n junction with a built-in electric field between two photocatalytic semiconductors has been proven to be capable of efficient photogenerated carriers separation, such as n-TiO_2/p-Ag_2O, n-TiO_2/p-NiO, n-ZnO/p-CuO_2, etc.[7] However, the photoreaction process tends to neutralize this electric field by rapid accumulation of charges. How to enhance the built-in electric field for enhancing photocatalytic activity of p–n heterostructured photocatalysts is still a great challenge.

Z. Liu, X. Zhang, M. Wu, Dr. L. Deng, Prof. L. Li, Prof. Z. L. Wang
Beijing Institute of Nanoenergy and Nanosystems
Chinese Academy of Sciences
Beijing 100083, P. R. China
E-mail: lilinlin@binn.cas.cn; zhong.wang@mse.gatech.edu

Z. Liu, X. Zhang, M. Wu, Dr. L. Deng, Prof. L. Li, Prof. Z. L. Wang
School of Nanoscience and Technology
University of Chinese Academy of Sciences
Beijing 100049, P. R. China

L. Wang, Dr. X. Yu, J. Zhang, R. Yang, Y. Ji
Institute for Advanced Interdisciplinary Research (iAIR)
University of Jinan
Jinan 250022, P. R. China
E-mail: ifc_yux@ujn.edu.cn

Prof. L. Li, Prof. Z. L. Wang
Center on Nanoenergy Research
School of Physical Science and Technology
Guangxi University
Nanning 530004, P. R. China

Prof. Z. L. Wang
School of Materials Science and Engineering
Georgia Institute of Technology Atlanta
GA 30332-0245, USA

**ADVANCED
SCIENCE NEWS**
www.advancedsciencenews.com

**ADVANCED
FUNCTIONAL
MATERIALS**
www.afm-journal.de

Recently, ferroelectric polarization and piezoelectric effect have been applied to generate a polar charge–created field for controlling carrier's separation in heterojunction.[8] When the piezoelectric material is polarized, the semiconductor material in the vicinity usually experiences a rapid shift in the distribution of free charge. At the same time, the depletion region's amplitude would be effectively regulated. Thus, it could fundamentally regulate the pattern of charge separation of the PEC electrode and enhance the oriented transmission of the electron–hole pairs.[9] Ferroelectric polarization and piezoelectric effect–enhanced photocatalysis has been observed in $TiO_2/BaTiO_3$, and $TiO_2/SrTiO_3$ core/shell nanowire photoanode.[10] By virtue of the piezoelectric properties, our previous study has also applied $BaTiO_3$ as an intercalation layer to enhance the carrier transport in Schottky junction between TiO_2 and Au for bacterial killing.[11] Additionally, a piezopotential field can be induced and regulated via purposely generated thermal stress, such as that proceed through heterogeneous cooling of the ZnO/TiO_2 heterostructure photocatalysts from different temperatures, namely utilizing the mismatched thermal expansion of the two types of materials.[12]

Inspired by these studies, for the first time, we have successfully used piezoelectric effect to enhance the PEC performance in p–n heterojunction. A multilayered $TiO_2/BTO/Ag_2O$ coaxial nanorod array was constructed as the photoanode, with a native piezoelectric field between n-TiO_2 and p-Ag_2O. Vertical nanorods represented an optimal architecture fitting for PEC water splitting, which had an impressive specific surface, low carrier recombination effect, and short carrier diffusion length. It was perpendicular to the charge collection substrate lying below, ensuring a relatively low level of recombination loss. p-Type Ag_2O with narrow bandgap (1.46 eV) broadened the light absorption from UV region to full UV–vis–NIR spectrum range.[13] The polar charge–created field induced by the polarized $BaTiO_3$ nanolayer can effectively promote the separation and suppress the recombination of the photocarriers generated by TiO_2 and Ag_2O. The solarcatalytic performance of the heterostructure was evaluated via the PEC performance under full solar spectrum from UV–vis to NIR light. The ternary hetero-nanorod array exhibited highly improved PEC activity and high stability. This work opens new avenues for developing p–n heterojunction for improving PEC performance with piezoelectric effect.

2. Results and Discussion

Figure 1a stepwisely illustrated the preparation process of the $TiO_2/BTO/Ag_2O$ photoanodes. Upon a fluorine-doped tin oxide (FTO) substrate, TiO_2 nanorod array was firstly grown out via a hydrothermal reaction.[14] Subsequently, the outermost nanolayer of the TiO_2 nanorods was transformed into a $BaTiO_3$ shell by in situ ion-exchange with barium precursor to form $TiO_2/BaTiO_3$ (TiO_2/BTO) core/shell nanorods. Outmost Ag_2O nanoparticles were generated via thermal annealing followed by spin-coating $AgNO_3$ layer onto the TiO_2/BTO surface. The finally fabricated 1D coaxial nanorod array structure had large specific surface area and a large number of active sites, both of which could contribute to the rapid electron transport. To endow the nanorods with positive polarization, the nanorod array was polarized with a +2 V voltage for 1 min in the 1 M NaOH aqueous electrolyte, with a Pt sheet counter electrode.[11] The polarized sample was denoted as $TiO_2/BaTiO_3/Ag_2O$ poling when compared with the samples without poling. If not specially mentioned, $TiO_2/BaTiO_3/Ag_2O$ denoted the sample with positive poling.

From scanning electron microscopy (SEM) images of the overall view (Figure 1b–d) and the corresponding cross-sectional view (Figure 1e,f), the FTO surface was uniformly coated with orderly oriented TiO_2 nanorods (Figure 1b,e for TiO_2 sample). The cubic and columnar TiO_2 nanorods were 50–150 nm in diameter, with a square top presenting a texture of small grids. After being converted into TiO_2/BTO core/shell heterostructure, the morphology of the nanorods had no change, but the surface became smoother, especially at the tip end of the original nanorods (Figure 1c,f). After Ag_2O was further loaded, a large number of particles, the diameter of which was about 20 nm, could be identified on the surface of the nanorods (Figure 1d,g). The nanorod length of TiO_2, TiO_2/BTO, and $TiO_2/BTO/Ag_2O$ was measured to be ≈3 μm. The high-resolution transmission electron microscope (HRTEM) image (Figure 1h) of the shell layer of the TiO_2/BTO nanorod indicated that it was composed of the characteristic tetragonal $BaTiO_3$ (lattice fringe $d_{103} = 0.34$ nm),[15] distinguishable from the interplanar distance ($d_{110} = 0.22$ nm) of naive TiO_2.[16] The thickness of the $BaTiO_3$ crust stratum was around 6–8 nm (Figure S6, Supporting Information), above the currently known critical thickness (≈2.4 nm) at which $BaTiO_3$ would show ferroelectricity under ambient conditions.[17] The TiO_2/BTO interface showed good crystalline lattice match, indicating high coherence across the interface. A large number of Ag_2O nanoparticles ($d_{200} = 0.24$ nm)[18] with an average diameter of ≈20 nm were uniformly distributed on the nanorod surface. In addition, energy dispersive X-ray (EDX) element mapping (Figure 1i) confirmed the core/shell/nanoparticle structure of $TiO_2/BTO/Ag_2O$.

From the X-ray diffraction (XRD) results (Figure S7, Supporting Information), 2θ peak diffraction at 26.5°, 37.9°, 51.7°, 61.7°, and 65.8° could be identified as corresponding to the (110), (200), (211), (310), and (301) faces of SnO_2 crystal (JCPDS No. 77-0451) of the FTO substrate.[19] The 2θ peak diffraction of 36.1°, 54.3°, 62.7°, 69.0°, 69.8°, and 76.5° was attributed to (101), (211), (002), (301), (112), and (201) planes of rutile TiO_2 (JCPDS No. 02-0494).[20] The 31.2° diffraction peak was from the (101) face of the tetragonal $BaTiO_3$ (JCPDS No. 05-0626).[21] The 54.9° and 65.4° peaks were assigned to cubic Ag_2O (JCPDS No. 41-1104).[22] From the Raman spectra, the peaks at 240, 445, and 608 cm^{-1} were from the TiO_2 nanorods, corresponding to the Raman active modes of hematite with the second order symmetries, E_g and A_{1g}, respectively (**Figure 2**a).[23] For the TiO_2/BTO heterostructure, an additional Raman peak at ≈305 cm^{-1} was assigned to the ferroelectric tetragonal phase of $BaTiO_3$.[24] Furthermore, peaks at around 774 and 1078 cm^{-1} could be related with the stretching of Ag-O bound in $TiO_2/BTO/Ag_2O$.[25]

The X-ray photoelectron spectroscopy (XPS) over the whole spectrum range showed that the $TiO_2/BTO/Ag_2O$ on FTO sample had no impurities, such as carbon residue (Figure S8, Supporting Information). The binding energies (BE) of 795.2 and 779.9 eV were Ba $3d_{3/2}$ and Ba $3d_{5/2}$, respectively, ascribed
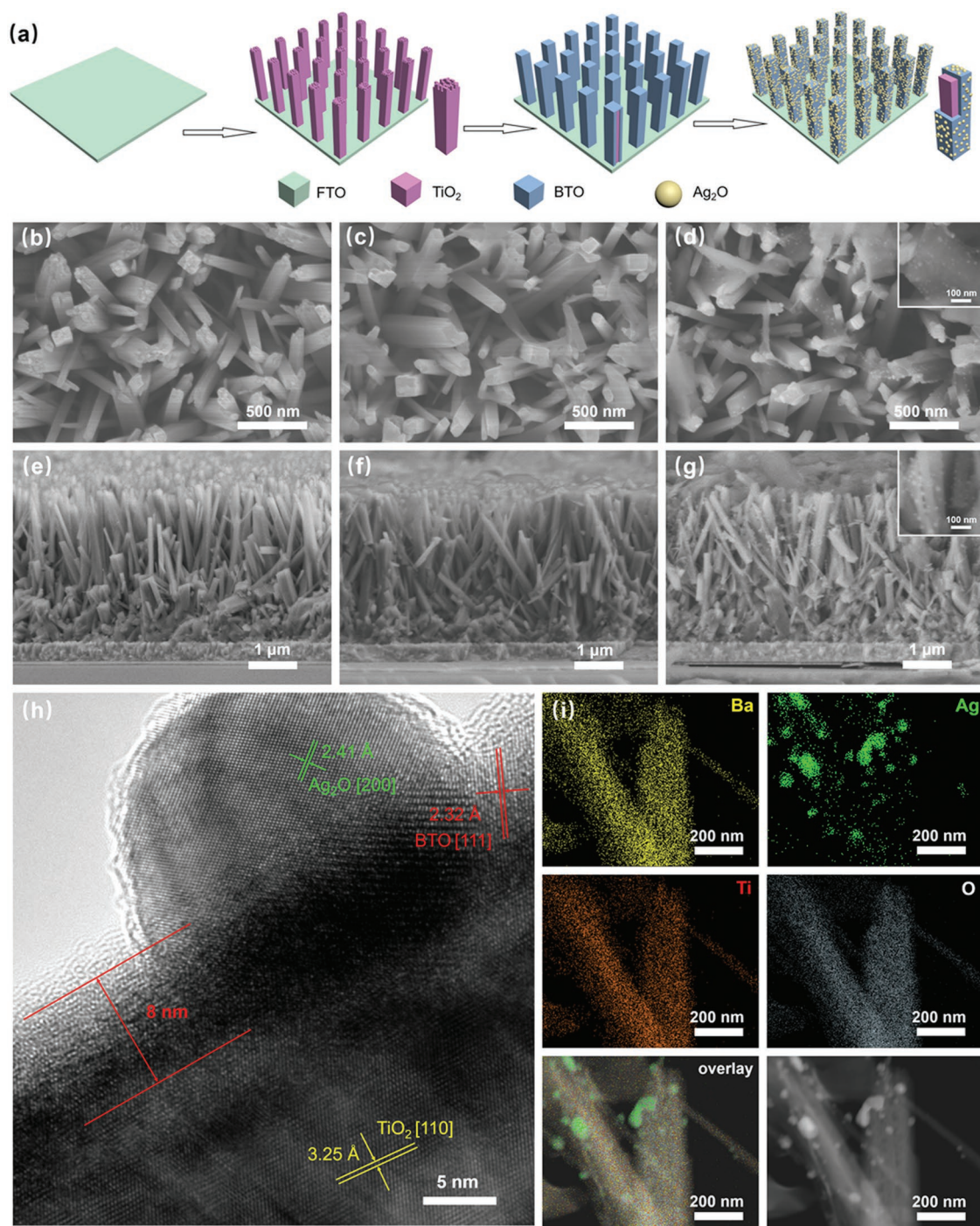
Figure 1. a) Scheme of the fabrication process of TiO$_2$/BTO/Ag$_2$O nanorod array. b–d) SEM images of top surface view, and e–g) cross-sectional view of b,e) TiO$_2$, c,f) TiO$_2$/BTO, and d,g) TiO$_2$/BTO/Ag$_2$O nanorod. h) HRTEM image and i) EDX element mapping of TiO$_2$/BTO/Ag$_2$O nanorod.

to the Ba^{2+} oxidation state (Figure 2b).[26] The 463.9 eV peak of Ti 2p$_{3/2}$ and that at 458.2 eV of Ti 2p$_{1/2}$ were from both TiO$_2$ and BaTiO$_3$ (Figure S8d, Supporting Information).[27] Ag 3d$_{3/2}$ and Ag 3d$_{5/2}$ peaks at 373.6 and 367.6 eV (Figure 2c) were consistent with the valence state of Ag$^+$.[28]

The TiO$_2$ and TiO$_2$/BTO nanorod absorbed UV light strongly, showing a sharp absorption peak and cutoff at around 380 nm (Figure 2d).[29] After the introduction of Ag$_2$O, a shoulder peak

appeared at ≈700 nm and the absorption extended to near-infrared (NIR) region up to 1200 nm for TiO$_2$/BTO/Ag$_2$O.[30] Thus, the full UV–vis–NIR photoelectrocatalysis could be expected to induce wide-range PEC responses.

Atomic force microscopic (AFM) morphological features of the TiO$_2$/BTO/Ag$_2$O heterostructure were consistent with that observed with SEM and TEM (Figure S9a,b, Supporting Information). Phase and amplitude of the piezoelectric
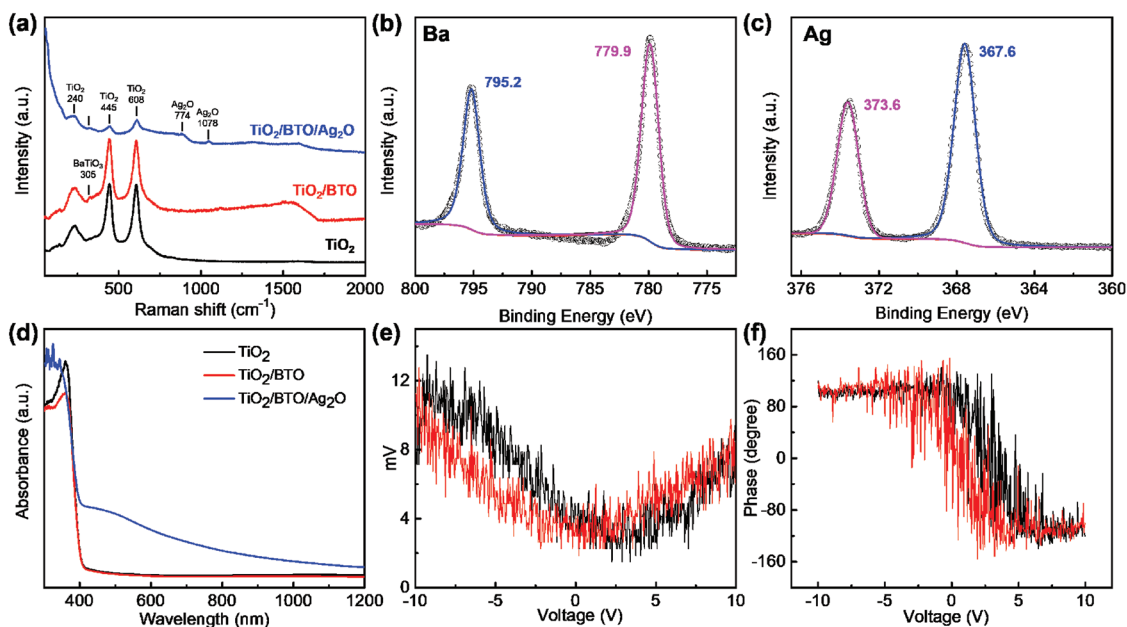
Figure 2. a) Raman spectra of TiO$_2$ nanorod, TiO$_2$/BTO nanorod, and TiO$_2$/BTO/Ag$_2$O nanorod. High-resolution XPS spectra for b) Ba 3d and c) Ag 4f. d) UV–vis diffuses reflectance spectra of the photoanodes. e) The standard ferroelectric amplitude curve and f) the phase curve obtained by applying a ramp voltage from −10 to 10 V of the TiO$_2$/BTO/Ag$_2$O nanorod.

response provided some information on the local piezoelectric feature, which can be induced by applying a direct current (DC) bias. The multilayered core–shell structured nanorod was interrogated with a 10 V voltage, resulting in an evident piezoelectricity (Figure S9c,d, Supporting Information). A looped voltage ramp, starting from −10 V and then ramping up to +10 V was applied, in order to obtain the well-established butterfly amplitude curve (Figure 2e) and phase curve (Figure 2f). Typical fluctuation in the butterfly amplitude curve was observed, suggesting that varied strain was experienced by the nanorods, and such constantly changed strain could be attributed to the applied external field. Such behavior could be viewed as the embodiment of the piezoelectric characteristic. On the phase chart, reversing the polarity of the external field induced ≈240° switching of the domain phase (Figure 2f), confirming the ferroelectric features of TiO$_2$/BTO/Ag$_2$O.[31]

Trapping techniques are a powerful in situ tool to ascertain the transiently active species involved in the photoelectrochemical reaction. Using common spin probes such as 5,5-dimethyl-1-pyrroline *N*-oxide (DMPO), 2,2,6,6-tetramethyl-1-piperidine (TEMP), and 2,2,6,6-tetramethylpiperidine-1-oxyl (TEMPO), the existence of superoxide (•$^-$O$_2$), hydroxyl radical (•OH), and singlet oxygen (^{1}O$_2$) could be confirmed by electron paramagnetic resonance (ESR), respectively.[32] These main reactive oxygen species could be produced by TiO$_2$, TiO$_2$/BTO, and TiO$_2$/BTO/Ag$_2$O under the Xe lamp light irradiation (Figure S11, Supporting Information). Most importantly, the TiO$_2$/BTO/Ag$_2$O after positive poling exhibited the highest ROS generation efficiency over all the other configurations, which was about 3.8-folds of TiO$_2$ alone, 2.3-folds of TiO$_2$/BTO, and 1.5-folds of TiO$_2$/BTO/Ag$_2$O without poling. Further, we tested the amount of free radical production of TiO$_2$/BTO/Ag$_2$O poling with prolonged time. As the irradiation time prolonged from 20 s,

40 s, to 60 s, the amount of •$^-$O$_2$, •OH, and ^{1}O$_2$ production was also gradually increased (Figure S11d–f, Supporting Information). These reactive oxygen species would play important roles in photocatalytic reaction process.[33]

PEC measurements were performed using TiO$_2$, TiO$_2$/BTO, and TiO$_2$/BTO/Ag$_2$O nanorod (with and without poling) as the photoanode, respectively. The as-constructed TiO$_2$/BTO/Ag$_2$O nanorod array exhibited relatively low transparency at the whole wavelength range. Therefore, in this work, all the PEC measurements were conducted with the light irradiation from the undercoated backside of the substrate. The photocurrent of the photoanodes was tested under UV, Vis, and NIR light irradiation, respectively. Under the UV light excitation (**Figure 3**a), TiO$_2$/BTO generated the highest photocurrent of 73 µA cm^{-2}, while the photocurrent intensity of TiO$_2$/BTO/Ag$_2$O slightly decreased to 60 µA cm^{-2}. This may be due to the fact that Ag$_2$O on the surface would combine with some electrons/holes, under the irradiation of UV light. However, the photocurrent for TiO$_2$/BTO/Ag$_2$O with poling (64 µA cm^{-2}) was still higher than that originally expected. This would be further discussed in the following paragraph. With the Vis and NIR light irradiation, TiO$_2$ and TiO$_2$/BTO exhibited a generally negligible photocurrent intensity. In comparison, under Vis light, TiO$_2$/BTO/Ag$_2$O without poling exhibited a good photoelectric response capability with a photocurrent density of ≈27 µA cm^{-2}, and that of TiO$_2$/BTO/Ag$_2$O after poling was further improved to 30 µA cm^{-2} (Figure 3b). Under the NIR light excitation (Figure 3c), TiO$_2$/BTO/Ag$_2$O can also generate electron–hole pairs. The photocurrent was about 2.0 µA cm^{-2} for the sample without poling and further increased to 3.5 µA cm^{-2} for the polarized one. Figure 3d shows the photocurrent in the full-spectrum simulated sunlight (100 mW cm^{-2} equipped with AM 1.5 filter). The photocurrent of the TiO$_2$/BTO/Ag$_2$O
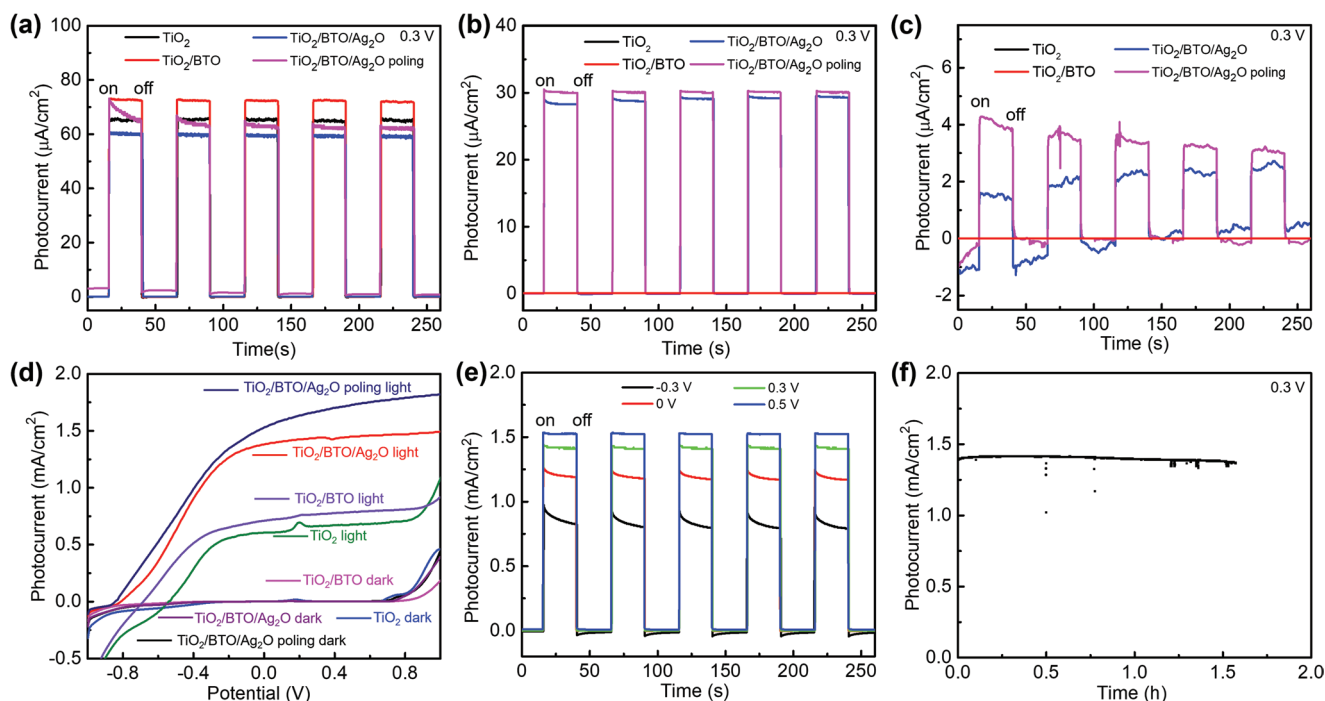
Figure 3. Photocurrent density ON–OFF curves under a) UV light, b) Vis light, and c) NIR light with a 0.3 V bias. d) Current–voltage (J–V) curve in the dark and under Xe lamp irradiation of the different photoanodes. e) Photocurrent densities versus time being applied with different bias potentials. f) Photochemical stability of the $TiO_2/BTO/Ag_2O$ photoanode with a 0.3 V bias under a Xe lamp.

poling as photoanode tested in the full-spectrum light reached to the highest 1.8 mA cm^{-2} at the bias of 0.8 V, which was about 1.2 times of $TiO_2/BTO/Ag_2O$ without poling, 2.2 times of TiO_2/BTO, and 2.6 times of TiO_2 nanorod photoanode. In addition, when −0.3, 0, 0.3, 0.5 V bias was applied to the $TiO_2/BTO/Ag_2O$ poling heterostructures, the photocurrent densities reached an average of 0.8, 1.2, 1.4, and 1.55 mA cm^{-2}, respectively (Figure 3e). The rapid and reversible photocurrent responses were attributed to the fact that carrier separation was improved by applied bias voltage. Furthermore, from the incident photo-to-electron conversion efficiency (IPCE) measurement (Figure S12, Supporting Information), the $TiO_2/BTO/Ag_2O$ heterostructures showed photoelectrocatalytic activity in a wide spectral range from the UV to the NIR light region (300–900 nm). And $TiO_2/BTO/Ag_2O$ poling had the higher

IPCE constantly than $TiO_2/BTO/Ag_2O$ without poling. The polarized nanorod array photoanode also had high stability during the solar-chemo-reaction process from the chrono-amperometric curve under 0.3 V bias and continuous Xe lamp agitation (Figure 3f). A slight initial decay was observed during the first 20 min, while the current density remained nearly unchanged over 1 h from then on (within 3% change).

For TiO_2, TiO_2/BTO, $TiO_2/BTO/Ag_2O$ without poling and polarized $TiO_2/BTO/Ag_2O$, electrochemical impedance spectra (EIS) had been recorded to study the charge transport behaviors near the heterojunction region (**Figure 4**). On a typical Nyquist diagram, interface charge transfer resistance usually appears as an arc or semicircle in the interface domain of the curve.[34] For the $TiO_2/BTO/Ag_2O$ poling in the darkness (Figure 4a) or under Xe lamp illumination (Figure 4b), diameter of the arc
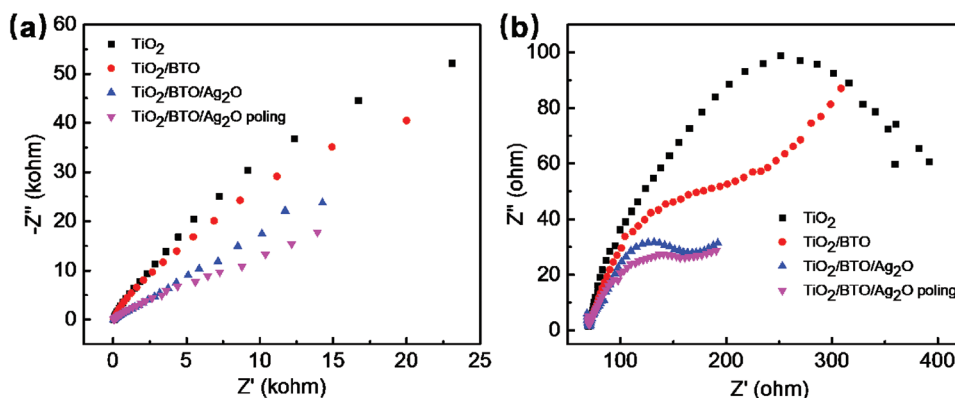

Figure 4. EIS Nyquist plots with a bias of 0 V a) under dark and b) Xe lamp light irradiation of different photoanodes.
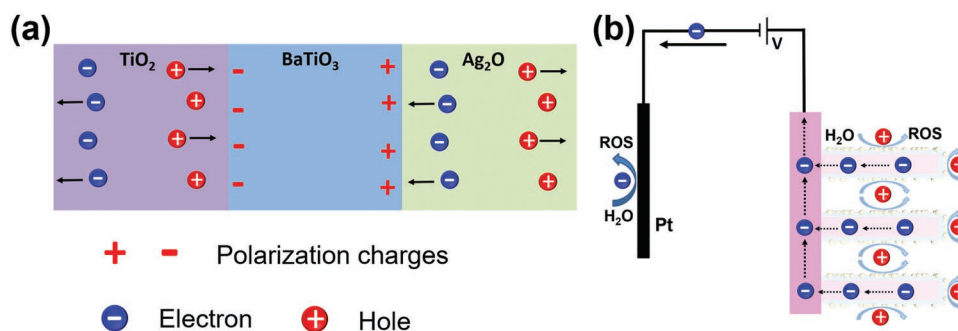
Figure 5. a) Schematic diagram of PEC activity under full-spectrum light illumination. b) Mechanism for the enhanced PEC performance for the TiO$_2$/BTO/Ag$_2$O poling.

was always smaller than those recorded for TiO$_2$, TiO$_2$/BTO and TiO$_2$/BTO/Ag$_2$O without poling. It proved the improved interface charge transfer of the polarized heterojunction. Further irradiation decreased the diameter of the EIS arc of TiO$_2$/BTO/Ag$_2$O poling, because the input of photo energy might further enhance the conductivity of the heterojunction. Furthermore, the TiO$_2$/BTO/Ag$_2$O after poling showed much lower intensity of the emission peak compared to the other samples (Figure S13, Supporting Information), indicating that the recombination of photoinduced electrons and holes was significantly prohibited. From the time-resolved photoluminescence (PL) decay spectra (Figure S14, Supporting Information), the TiO$_2$/BTO/Ag$_2$O after poling had the longest fluorescence lifetime value of 34.47 ns (Table S1, Supporting Information). The prolonged fluorescence lifetime was related to a long life of electrons in the excited state, which was highly desirable for the migration and surface reaction of photogenerated charge carriers.

Based on these data, the mechanism is deduced as follows. Electrons and holes are generated by photons both in TiO$_2$ and Ag$_2$O.[35] After the BTO is polarized, the piezoelectric charges created at the two sides of BTO nanolayer could maintain carrier–pair separation in n-TiO$_2$ and p-Ag$_2$O more efficiently.[36] The n-type carriers in TiO$_2$ would partially screen the holes in TiO$_2$, while the p-type carriers in Ag$_2$O would partially screen the electrons in Ag$_2$O.[37] For the details, as illustrated in **Figure 5**a, to the left-hand side of BTO, the piezoelectric-induced negative charges would attract holes in TiO$_2$; whereas to the right-hand side of BTO, the corresponding positive charges would attract the electrons in Ag$_2$O. In the TiO$_2$ core, the electrons could flow toward the conductive FTO substrate along the TiO$_2$ monocrystal nanorods, which constitutes a highway for the charge transfer. At last, the electrons would reach the Pt counter electrode under the external electrostatic field (Figure 5b).

When the TiO$_2$/BTO/Ag$_2$O is illuminated under the full-spectrum light, TiO$_2$ can harvest light in the UV range, whereas the Vis + NIR light can reach Ag$_2$O nanoparticles and be absorbed, thus realizing a full-spectrum utilization of the incoming light. The insertion of BaTiO$_3$ nanolayer between p-Ag$_2$O and n-TiO$_2$ could form a piezopotential, which could greatly promote the electron–hole separation, facilitate the charge transport and prolong the lifetime of carriers.[38] This is termed piezophototronic effect in piezoelectric-semiconductor materials, and this effect could significantly enhance their optoelectronic performances.[39]

Under the irradiation of single resource UV light, most of the photons would be absorbed by TiO$_2$ due to the shallow penetration depth of the UV light, and almost no light can reach Ag$_2$O. Electron–hole pairs would be generated after TiO$_2$ absorbs the photons. However, with Ag$_2$O nanoparticles on the surface of the nanorods, there are many free electrons and holes in Ag$_2$O, which would recombine the carriers to a certain extent. It is the cause that compared with the TiO$_2$/BTO photoanode, TiO$_2$/BTO/Ag$_2$O had a slightly decreased photocurrent under the UV light (Figure 3a). Similarly, under the irradiation of Vis + NIR light, the light might pass through the TiO$_2$ and BaTiO$_3$ and reach Ag$_2$O nanoparticles for photoactivation. When Ag$_2$O is excited, it would produce photogenerated carriers. However, it would be hard for the photogenerated electrons to pass through TiO$_2$ and BaTiO$_3$ to reach the photocathode. Although the vertically oriented monocrystal TiO$_2$ has a strong electron transporting capability, holes existing in the rod body would still recombine a portion of the electrons. Therefore, under only the Vis + NIR light irradiation, the photocurrent is not very high (Figure 3b,c). Fortunately, with a full-spectrum light, the piezoelectric effect could greatly increase the PEC performance.

3. Conclusion

In summary, an effective piezoelectric effect–enhanced photoelectrocatalyst has been successfully fabricated by inserting a BaTiO$_3$ nanolayer between n-TiO$_2$ and p-Ag$_2$O to form multilayered coaxial nanorod array as the photoanode. Particularly, the greatly augmented carrier separation was contributed from the BaTiO$_3$ inserting layer, which generated a piezoelectric effect–induced internal electric field at the n-TiO$_2$ and p-Ag$_2$O interface. This polar charge–created field could decrease the recombination of carriers for a longer lifetime and improve the PEC performance. Potential solar-electric energy harvesting and conversion devices may further extend the application and demonstrate the feasibility of the unique strategy.

Supporting Information

Supporting Information is available from the Wiley Online Library or from the author.

[1] a) R. Tang, S. Zhou, Z. Yuan, L. Yin, *Adv. Funct. Mater.* **2017**, *27*, 1701102; b) F. Ning, M. Shao, S. Xu, Y. Fu, R. Zhang, M. Wei, D. G. Evans, X. Duan, *Energy Environ. Sci.* **2016**, *9*, 2633; c) Z. Luo, T. Wang, J. Zhang, C. Li, H. Li, J. Gong, *Angew. Chem., Int. Ed.* **2017**, *56*, 12878.

[2] a) A. Fujishima, K. Honda, *Nature* **1972**, *238*, 37; b) Y. Zhao, X. Jia, G. Chen, L. Shang, G. I. N. Waterhouse, L. Wu, C. Tung, D. O'Hare, T. Zhang, *J. Am. Chem. Soc.* **2016**, *138*, 6517.

[3] a) X. Yu, Z. Zhao, D. Sun, N. Ren, J. Yu, R. Yang, H. Liu.*Appl. Catal., B* **2018**, *227*, 470; b) H. Huang, S. Tu, C. Zeng, T. Zhang, A. H. Reshak, Y. Zhang, *Angew. Chem., Int. Ed.* **2017**, *129*, 12022; c) S. Wang, T. He, J. Yun, Y. Hu, M. Xiao, A. Du, L. Wang, *Adv. Funct. Mater.* **2018**, *28*, 1802685.

[4] a) T. Ji, Q. Liu, R. Zou, Y. Sun, K. Xu, L. Sang, M. Liao, Y. Koide, L. Yu, J. Hu, *Adv. Funct. Mater.* **2016**, *26*, 1400; b) W. Wang, J. Dong, X. Ye, Y. Li, Y. Ma, L. Qi, *Small* **2016**, *12*, 1469; c) C. Chen, Y. Wei, G. Yuan, Q. Liu, R. Lu, X. Huang, Y. Cao, P. Zhu, *Adv. Funct. Mater.* **2017**, *27*, 1701575.

[5] a) J. Liu, X. Yu, Q. Liu, R. Liu, X. Shang, S. Zhang, W. Li, W. Zheng, G. Zhang, H. Cao, Z. Gu, *Appl. Catal., B* **2014**, *158*, 296; b) Y. Wang, X. Liu, Z. Li, Y. Tao, Y. Li, X. Liu, S. Jia, Y. Zhao, *Small* **2017**, *13*, 1700793.

[6] a) L. Zhu, H. Lu, D. Hao, L. Wang, Z. Wu, L. Wang, P. Li, J. Ye, *ACS Appl. Mater. Interfaces* **2017**, *9*, 38537; b) Y. Hou, X. Li, Q. Zhao, X. Quan, G. Chen, *Adv. Funct. Mater.* **2010**, *20*, 2165; c) X. Yu, Z. Zhao, N. Ren, J. Liu, D. Sun, L. Ding, H. Liu. *ACS Sustainable Chem. Eng.* **2018**, *6*, 11775; d) L. Wang, N. T. Nguyen, X. Huang, P. Schmuki, Y. Bi, *Adv. Funct. Mater.* **2017**, *27*, 1703527.

[7] a) D. Sarkar, C. K. Ghosh, S. Mukherjee, K. K. Chattopadhyay, *ACS Appl. Mater. Interfaces* **2013**, *5*, 331; b) X. Yu, J. Zhang, Z. Zhao, W. Guo, J. Qiu, X. Mou, A. Li, J. P. Claverie, H. Liu, *Nano Energy* **2015**, *16*, 207; c) Z. Kang, X. Yan, Y. Wan1, Z. Bai, Y. Liu, Z. Zhang, P. Lin, X. Zhang, H. Yuan, X. Zhang, Y. Zhang, *Sci. Rep.* **2015**, *5*, 7882.

[8] S. Singh, N. Khare, *Nano Energy* **2017**, *38*, 335.

[9] a) T. Choi, S. Lee, Y. J. Choi, V. Kiryukhin, S.-W. Cheong, *Science* **2009**, *324*, 63; b) I. Grinberg, D. V. West, M. Torres, G. Gou, D. M. Stein, L. Wu, G. Chen, E. M. Gallo, A. R. Akbashev, P. K. Davies, J. E. Spanier, A. M. Rappe, *Nature* **2013**, *503*, 509.

[10] a) F. Wu, Y. Yu, H. Yang, L. N. German, Z. Li, J. Chen, W. Yang, L. Huang, W. Shi, L. Wang, X. Wang, *Adv. Mater.* **2017**, 1701432; b) W. Yang, Y. Yu, M. B. Starr, X. Yin, Z. Li, A. Kvit, S. Wang, P. Zhao, X. Wang, *Nano Lett.* **2015**, *15*, 7574.

[11] X. Yu, S. Wang, X. Zhang, A. Qi, X. Qiao, Z. Liu, M. Wu, L. Li, Z. L. Wang, *Nano Energy* **2018**, *46*, 29.

[12] L. Wang, S. Liu, Z. Wang, Y. Zhou, Y. Qin, Z. L. Wang, *ACS Nano* **2016**, *10*, 2636.

[13] a) C. Liu, C. Cao, X. Luo, S. Luo, *J. Hazard. Mater.* **2015**, *285*, 319; b) P. Mazierski, A. Malankowska, M. Kobylański, M. Diak, M. Kozak, M. J. Winiarski, T. Klimczuk, W. Lisowski, G. Nowaczyk, A. Zaleska-Medynska, *ACS Catal.* **2017**, *7*, 2753.

[14] X. Yu, Z. Zhao, J. Zhang, W. Guo, J. Qiu, D. Li, Z. Li, X. Mou, L. Li, A. Li, H. Liu, *Small* **2016**, *12*, 2759.

[15] Y. Cui, J. Briscoe, Y. Wang, N. Tarakina, S. Dunn, *ACS Appl. Mater. Interfaces* **2017**, *9*, 24518.

[16] a) X. Hou, X. Wang, B. Liu, Q. Wang, Z. Wang, D. Chen, G. Shen, *Small* **2014**, *1*, 108; b) X. Yu, X. Han, Z. Zhao, J. Zhang, W. Guo, C. Pan, A. Li, H. Liu, Z. L. Wang, *Nano Energy* **2015**, *11*, 19.

[17] M. Trieloff, E. K. Jessberger, I. Herrwerth, J. Hopp, C. Fiéni, M. Ghélis, M. Bourot-Denise, P. Pellas, *Nature* **2003**, *422*, 502.

[18] H. Li, T. Chen, Y. Wang, J. Tang, Y. Wang, Y. Sang, H. Liu, *Chin. J. Catal.* **2017**, *38*, 1063.

[19] X. Wang, Y. Sang, D. Wang, S. Ji, H. Liu, *J. Alloys Compd.* **2015**, *639*, 571.

[20] a) P. Yan, X. Wang, X. Zheng, R. Li, J. Han, J. Shi, A. Li, Y. Gan, C. Li, *Nano Energy* **2015**, *15*, 406; b) D. E. Schipper, Z. Zhao, A. P. Leitner, L. Xie, F. Qin, M. K. Alam, S. Chen, D. Wang, Z. Ren, Z. Wang, *ACS Nano* **2017**, *11*, 4051.

[21] a) X. Zhang, Y. Shen, Q. Zhang, L. Gu, Y. Hu, J. Du, Y. Lin, C. Nan, *Adv. Mater.* **2015**, *27*, 819; b) T. Yim, S. Han, N. Park, M. Park, J. Lee, J. Shin, J. Choi, Y. Jung, Y. Jo, J. Yu, K. Kim. *Adv. Funct. Mater.* **2016**, *26*, 7817.

[22] a) C. Yu, G. Li, S. Kumar, K. Yang, R. Jin, *Adv. Mater.* **2014**, *26*, 892; b) D. P. Kumar, N. L. Reddy, M. Karthik, B. Neppolian, J. Madhavan, M. V. Shankar, *Sol. Energy Mater. Sol. Cells* **2016**, *154*, 78.

[23] M. Ye, D. Zheng, M. Wang, C. Chen, W. Liao, C. Lin, Z. Lin, *ACS Appl. Mater. Interfaces* **2014**, *6*, 2893.

[24] A. P. Espinosa, J. Camargo, A. Campo, F. R. Marcos, M. Castro, L. Ramajo, *J. Alloys Compd.* **2018**, *739*, 799.

[25] a) Y. Cui, Q. Ma, X. Deng, Q. Meng, X. Cheng, M. Xie, X. Li, Q. Cheng, H. Liu, *Appl. Catal., B* **2017**, *206*, 136; b) C. Li, C. Yang, S. Xu, C. Zhang, Z. Li, X. Liu, S. Jiang, Y. Hou, A. Liu, B. Man, *J. Alloys Compd.* **2017**, *695*, 1677.

[26] D. Zhong, W. Liu, P. Tan, A. Zhu, Y. Liu, X. Xiong, J. Pan, *Appl. Catal., B* **2018**, *227*, 1.

[27] a) X. Yu, Z. Zhao, D. Sun, N. Ren, L. Ding, R. Yang, Y. Ji, L. Li, H. Liu, *Chem. Commun.* **2018**, *54*, 6056; b) X. Yu, L. Wang, J. Zhang, W. Guo, Z. Zhao, Y. Qin, X. Mou, A. Li, H. Liu, *J. Mater. Chem. A* **2015**, *3*, 19129.

[28] Y. Cui, Q. Ma, X. Deng, Q. Meng, X. Cheng, M. Xie, X. Li, Q. Cheng, H. Liu, *Appl. Catal., B* **2017**, *26*, 136.

[29] a) X. Yu, N. Ren, J. Qiu, D. Sun, L. Li, H. Liu, *Sol. Energy Mater. Sol. Cells* **2018**, *183*, 41; b) X. Yu, Z. Zhao, J. Zhang, W. Guo, L. Li, H. Liu, Z. L. Wang. *CrystEngComm* **2017**, *19*, 129; c) R. Li, Q. Li, L. Zong, X. Wang, J. Yang, *Electrochim. Acta* **2013**, *91*, 30.

[30] X. Zhao, Y. Su, X. Qi, X. Han, *ACS Sustainable Chem. Eng.* **2017**, *5*, 6148.

[31] a) S. Li, J. Zhang, B. Zhang, W. Huang, C. Harnagea, R. Nechache, L. Zhu, S. Zhang, Y. Lin, L. Ni, Y. Sang, H. Liu, F. Rosei, *Nano Energy* **2017**, *35*, 92; b) L. Zhao, Y. Zhang, F. Wang, S. Hu, X. Wang, B. Ma, H. Liu, Z. L. Wang, Y. Sang, *Nano Energy* **2018**, *39*, 461.

[32] Y. Liu, H. Wu, M. Li, J. Yin, Z. Nie, *Nanoscale* **2014**, *6*, 11904.

[33] D. Liu, J. Wang, X. Bai, R. Zong, Y. Zhu, *Adv. Mater.* **2016**, *28*, 7284.

[34] D. E. Schipper, Z. Zhao, A. P. Leitner, L. Xie, F. Qin, M. K. Alam, S. Chen, D. Wang, Z. Ren, Z. Wang, J. Bao, K. H. Whitmire, *ACS Nano* **2017**, *11*, 4051.

[35] W. Zhou, H. Liu, J. Wang, D. Liu, G. Du, J. Cui, *ACS Appl. Mater. Interfaces* **2010**, *2*, 2385.

[36] H. Li, Y. Sang, S. Chang, X. Huang, Y. Zhang, R. Yang, H. Jiang, H. Liu, Z. L. Wang, *Nano Lett.* **2015**, *15*, 2372.

[37] a) G. Bhalla, C. Bell, J. Ravichandran, W. Siemons, Y. Hikita, S. Salahuddin, A. Hebard, H. Hwang, R. Ramesh, *Nat. Phys.* **2011**, *7*, 80; b) R. Su, Y. Shen, L. Li, D. Zhang, G. Yang, C. Gao, Y. Yang,

Small **2015**, *11*, 202; c) M. Stock, S. Dunn, *J. Phys. Chem. C* **2012**, *116*, 20854.

[38] a) Y. Cui, J. Briscoe, S. Dunn, *Chem. Mater.* **2013**, *25*, 4215; b) C. Bowen, H. Kim, P. Weaver, S. Dunn, *Energy Environ. Sci.* **2014**, *7*, 25.

[39] a) Z. L. Wang, *Mater. Today* **2010**, *5*, 540; b) X. Li, M. Chen, R. Yu, T. Zhang, D. Song, R. Liang, Q. Zhang, S. Cheng, L. Dong, A. Pan, Z. L. Wang, J. Zhu, C. Pan, *Adv. Mater.* **2015**, *30*, 4447; c) C. Pan, L. Dong, G. Zhu, A. Niu, R. Yu, Q. Yang, Y. Liu, Z. L. Wang, *Nat. Photonics* **2013**, *7*, 752.

1807279 (8 of 8)